How to cite: *Angew. Chem. Int. Ed.* **2023**, *62*, e202303268
doi.org/10.1002/anie.202303268

Bioelectrochemistry Hot Paper

An Implantable Fiber Biosupercapacitor with High Power Density by Multi-Strand Twisting Functionalized Fibers

Zheyan Qian, Yiqing Yang, Liyuan Wang, Jiajia Wang, Yue Guo, Ziwei Liu, Jianzheng Li, Haoyu Zhang, Xuemei Sun, and Huisheng Peng**

Abstract: Biosupercapacitors (BSCs) that can harvest and store chemical energy show great promise for power delivery of biological applications. However, low power density still limits their applications, especially as miniaturized implants. Here, we report an implantable fiber BSC with maximal power density of 22.6 mW cm^{-2}, superior to the previous reports. The fiber BSC was fabricated by integrating anode and cathode fibers of biofuel cell with supercapacitor fibers through multi-strand twisting. This twisting structure endowed many channels inside and high electrochemical active area for efficient mass diffusion and charge transfer among different fibers, benefiting high power output. The obtained thin and flexible fiber BSC operated stably under deformations and performed high biocompatibility after implantation. Eventually, the fiber BSC was implanted subcutaneously in rats and successfully realized electrical stimulation of sciatic nerve, showing promise as a power source in vivo.

Introduction

In recent years, flourishing implantable bioelectronic devices have gradually demonstrated their promising applications in health diagnosis, physiological monitoring and disease treatment. Energy supply in vivo is crucial to their development.[1] Among the emerging implantable energy devices, biofuel cells can directly convert chemical energy into electricity based on mild and sustainable reactions, while possess low power density.[2] Supercapacitors show high power density but are difficult to be recharged after implantation.[3] Developing hybrid devices with both energy harvesting and storing functions is an effective way to solve these problems. Biosupercapacitor (BSC) is proposed as a combination of biofuel cells and supercapacitors,[4] which can self-charge using biofuel energy and provide higher power output than standalone biofuel cell.[5] Therefore, BSCs have attracted considerable attentions in the field of biomedical devices.[6] Although BSCs have been widely demonstrated as wearable energy devices[7] and sensors,[8] it is rare for their applications in vivo, especially in implantable electronics that require high power transmission.

As for their implantation applications, miniaturization was always expected to reduce tissue damage and inflammation,[9] which would require high power density of BSC in order to provide sufficient power supply for implantable electronics[10] (i.e., cardiac pacemaker and nerve/muscle stimulator). However, currently reported BSCs[11] shared a bulky structure and showed power densities under 1 mW cm^{-2}. It was possibly due to low efficiencies of mass diffusion and charge transfer among different electrodes in BSCs.[12] The power density would be even reduced in physiological environments with low concentrations of biofuels.[13] Therefore, BSC with both tiny structure and high power density is essential while has not been realized yet to satisfy the requirements for implantable electronics.

Here, we demonstrated an implantable fiber BSC with high power density. It was fabricated by multi-strand twisting energy harvesting and storing modules based on carbon nanotube (CNT) fibers. The novel integration structure endowed the BSC with multiple channels and high electrochemical active surface area for efficient mass diffusion and charge transfer among electrodes. The fiber BSC delivered high power density of 22.6 mW cm^{-2} in a 4 mM glucose solution matching with the physiological range (3.9–7.8 mM), which much exceeds the previous reports.[4a,11] Also, the fiber BSC performed high electrochemical stability under continuous pulses and dynamic deformations. After being implanted into subcutaneous tissue of rat, the fiber BSC showed high biocompatibility and could realize effective electrical stimulation of the sciatic nerve.

Results and Discussion

The fiber BSC was achieved through integrating different functionalized modules, which were separately fabricated on CNT fibers (Figure 1a, b). Firstly, due to wide availability of glucose and oxygen in living bodies, we constructed glucose/oxygen biofuel cells toward implantation. Glucose oxidase (GOx) and tetrathiafulvalene (TTF), as glucose oxidizer and

[*] Z. Qian, Y. Yang, Dr. L. Wang, J. Wang, Y. Guo, Z. Liu, H. Zhang, Prof. X. Sun, Prof. H. Peng
State Key Laboratory of Molecular Engineering of Polymers, Department of Macromolecular Science and Laboratory of Advanced Materials, Fudan University
Shanghai 200438 (China)
E-mail: sunxm@fudan.edu.cn
penghs@fudan.edu.cn
J. Li
School of Information Science and Technology, Fudan University
Shanghai 200433 (China)

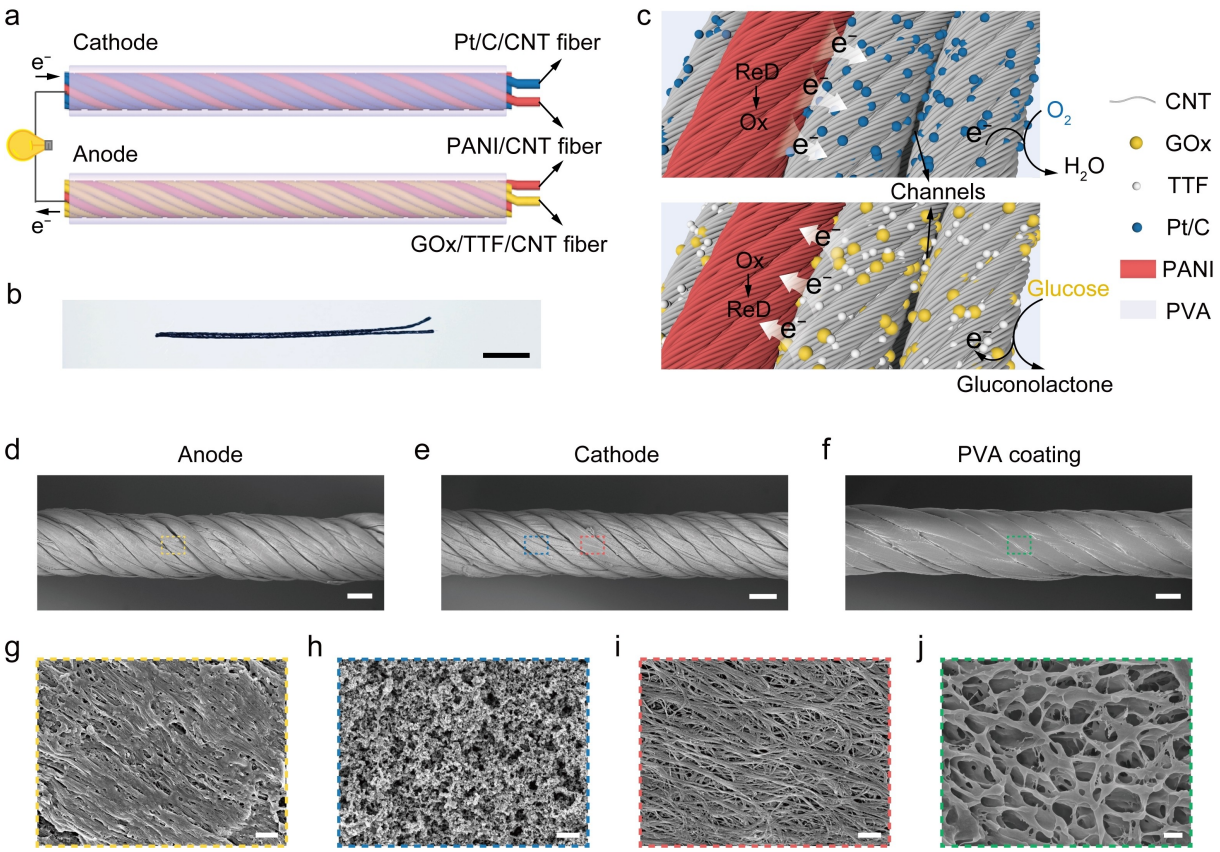

Figure 1. Schematic diagram and morphology of the fiber BSC. a) Schematic diagram of the construction of the fiber BSC. b) Photograph of the fiber BSC. Scale bar, 5 mm. c) Schematic diagram of working mechanisms of the fiber BSC. d)–f) SEM images of bare fiber anode, cathode and PVA-coated electrode. Scale bar, 100 μm. g)–j) High-magnification SEM images in (d)–(f) to show GOx/TTF/CNT (g), Pt/C/CNT (h), PANI/CNT (i) and PVA (j). Scale bar, g) 1 μm; h) 0.2 μm; i) 1 μm; j) 0.5 μm.

electron transfer mediator,[14] were coated on CNT fibers as the anode of biofuel cell, while platinum on carbon (Pt/C) as the catalyst for oxygen reduction[15] was assembled on CNT fibers as the cathode. Besides, polyaniline (PANI) with simultaneously high conductivity, pseudocapacitance and biocompatibility, was electrodeposited on CNT fibers as supercapacitors.[16] The diameter of each single functional electrode was about 70 μm and all modifications were uniform and dense (Figures 1g–i and S1). By twisting GOx/TTF/CNT and Pt/C/CNT fibers with PANI/CNT fibers (Figure S2), we obtained the fiber BSC. These electrodes with diameters of around 300 μm appeared as homogeneous and compact fibers with abundant micron-sized channels (Figures 1d, e and S3).

Such microchannels introduced by the integration of multiple twisted fibers facilitated mass diffusion and charge transfer.[17] During the operation of fiber BSC, glucose and oxygen in the environment could fully diffuse into the fiber along the microchannels. It allowed more reaction surfaces[18] with GOx and Pt/C to provide sufficient energy. Due to the potential difference between different functional modules, the charge generated by the redox reaction on GOx/TTF/CNT or Pt/C/CNT fibers would be preferentially transferred to the nearby twisted PANI/CNT fibers under open circuit (Figure 1c). Here, the multi-strand twisting of the fiber BSC made a tight and sufficient contact between the energy harvesting and storing fibers, providing abundant high-efficiency electron transfer pathways without additional external circuit connections. Therefore, the supercapacitors obtained high-flux charge transfer and stored it through the mechanism of pseudocapacitance.[19] Finally, when the circuit was connected, the fiber BSC would discharge at a high current pulse, releasing huge energy.

At the final step of the device preparation, polyvinyl alcohol (PVA) with high hydrophilicity and biocompatibility[20] was modified on the electrode via dip-coating and then converted into a gel layer with the thickness of about 6 μm via freeze crosslinking[21] (Figures 1f and S4). The gel allowed two fiber BSC electrodes to be closely placed in parallel (Figures 1b and S5), preventing short circuits and improving operational stability and reliability.

Energy harvesting and storing capability of the fiber BSC were characterized separately. For the energy harvesting module, as shown in linear sweep voltammograms, the anodic and cathodic currents increased along with the glucose and oxygen concentrations respectively (Figure 2a, b), demonstrating efficient occurrence of redox reactions and successful construction of biofuel cell. The power density-voltage curve also expanded outward as the

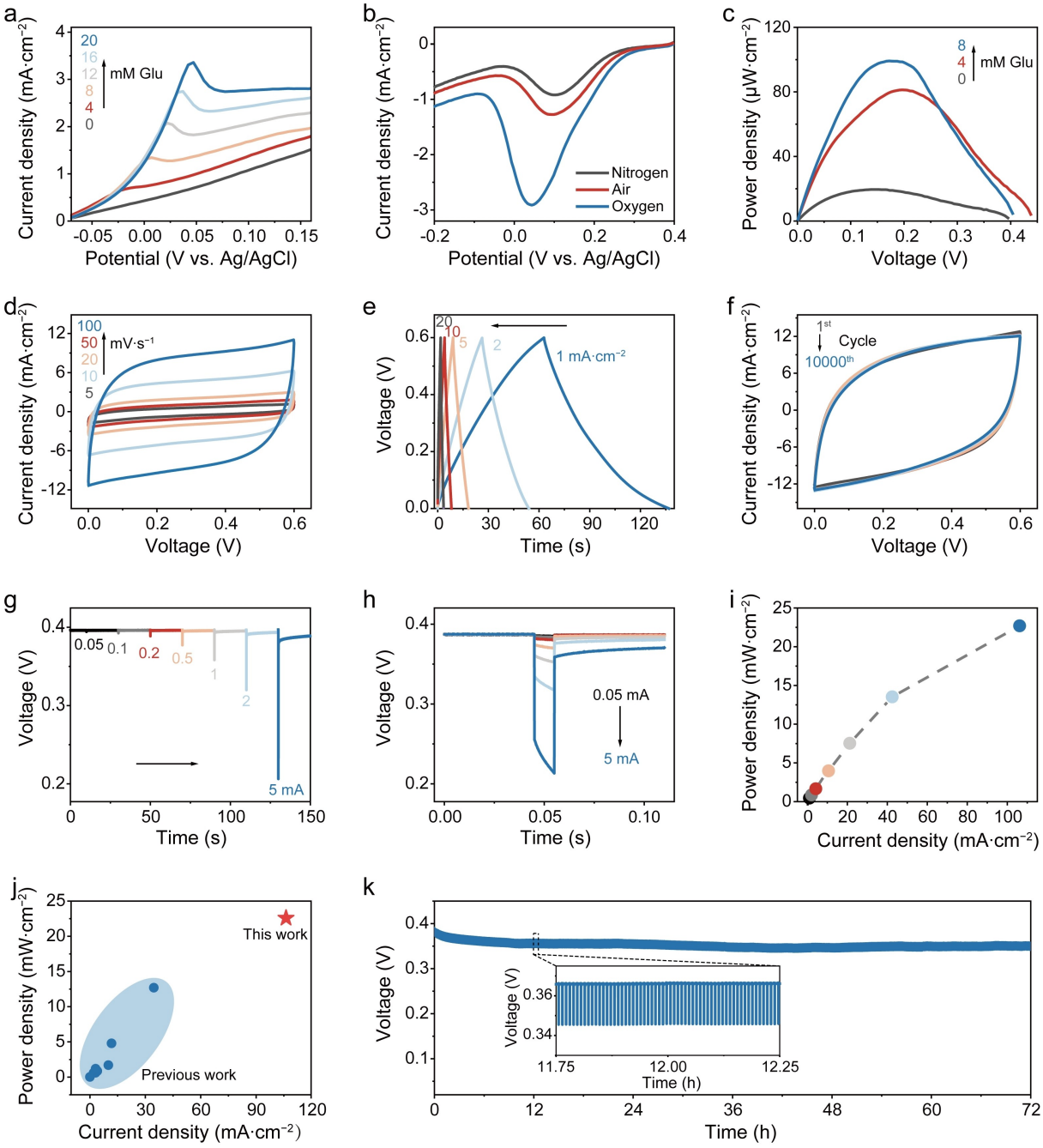

Figure 2. Electrochemical performance of fiber BSC. a) Linear sweep voltammograms of GOx/TTF/CNT fiber in 0–20 mM concentrations of glucose at 5 mV s^{-1}. b) Linear sweep voltammograms of Pt/C/CNT fiber in nitrogen-saturated, air-saturated and oxygen-saturated phosphate buffer saline (PBS) at 5 mV s^{-1}. c) Power density-voltage curves of the biofuel cell in 0–8 mM concentrations of glucose with a sweep rate of 5 mV s^{-1}. d) Cyclic voltammograms of fiber BSC at sweep rates of 5–100 mV s^{-1}. e) Galvanostatic charge-discharge curves of fiber BSC with current densities of 1–20 mA cm^{-2}. f) Evolution of cyclic voltammograms of fiber BSC after 10000 cycles at 100 mV s^{-1}. g) Pulse discharge curves of fiber BSC at current values of 0.05–5 mA. h) Overlay of the fiber BSC peak potential drop. i) Calculated pulse power density of fiber BSC at different discharge current densities. j) Comparison of areal power density and current density of our work with previously reported BSCs (Table S3). k) Recording of long-term pulse discharge of fiber BSC at 0.5 mA and local magnification (inset).

glucose concentration increased from 0 to 8 mM. The maximal power density reached 81.2 μW cm^{-2} at 4 mM glucose and 99.1 μW cm^{-2} at 8 mM glucose (Figure 2c). The maximal power density could be maintained by 94.9 % during 24 hours and over 70 % after three days (Figure S6). Moreover, there was no significant difference observed in the catalytic currents of the device with or without PVA coating (Figure S7), indicating that the thin and porous PVA-modified layer (Figure 1j) had negligible effects on the mass or charge transfer process.

Furthermore, the twisted multi-stranded fiber biofuel cell showed higher catalytic current density and power density than the single-stranded device (Figure S8). And the catalytic current densities were found to increase linearly with the number of twisted electrodes (Figure S9). It was mainly attributed to the microchannels generated by fiber twisting, which promoted sufficient utilization of interior space of electrodes and diffusions of glucose and oxygen, thereby leading to larger active reaction area[22] and higher catalytic activity. As shown in the impedance spectra, the twisted fiber electrode exhibited a higher slope at intermediate frequencies compared to the untwisted electrode, representing its lower diffuse layer resistance[23] (Figure S10).

For the energy storing module of fiber BSC, the content of PANI on CNT fibers was optimized by adjusting reaction charges during its electrodeposition at first. The fiber electrode with 50 wt % PANI was finally selected as the main component of the fiber BSC due to its uniform morphology and superior capacitance (Figures 1i and S11). Cyclic voltammograms of the fiber BSC exhibited a linear region over 0–0.6 V (Figure 2d), similar to that of PANI supercapacitor (Figure S12). Symmetric triangular charge-discharge behavior was observed at all current densities in galvanostatic charge-discharge tests (Figure 2e), showing high reversible pseudocapacitive behavior of the fiber BSC. It also displayed good rate capability with high specific capacitance of 123 $mF\,cm^{-2}$ at 1 $mA\,cm^{-2}$ (Figure S13), providing a solid foundation for high current discharge (Table S1). After 10 000 cycles scanning at 100 $mV\,s^{-1}$, the fiber BSC lost only 4.2 % of its capacitance (Figure 2f), demonstrating its exceptional cycling stability. In addition, the consistency of the fabrication process for different functional modules was characterized. The standard deviations of the performances could be reduced to as low as 2.46 % (Figure S14), ensuring the performance reproducibility of the fiber BSCs after integration.

The pulse discharge performance of the hybrid device was characterized via chronopotentiometry (Figure S15). In this test, the main contribution of the discharge current comes from the stored charge in supercapacitor. Higher capacitance enables the device to discharge at higher current.[24] However, as the number of supercapacitors increases, influence of the increased amount of pseudocapacitive material on the maximum open circuit voltage (OCV) and effective power output cannot be ignored[25] (Figure S16a). Therefore, the composition ratio of biofuel cells and supercapacitors was regulated to obtain optimized performance. The same GOx/TTF/CNT and Pt/C/CNT fibers were both combined with 0–5 PANI/CNT fibers to analyze the performance variation of the combined BSCs. The overall capacitance ranged from 0.68 to 7.34 mF (Table S2). Pulse discharge curves showed that the OCV of the BSC dropped obviously with the increasing combined PANI/CNT fibers (Figure S16b), due to the increasing leakage current.[26] However, at the same time, more PANI/CNT fibers resulted in a smaller capacitive discharge voltage drop and a higher pseudocapacitance shift drive,[27] allowing higher pulse discharge current and faster recovery after each discharge. OCV of the BSC with a capacitance of 7.34 mF recovered to 91.21 % of the initial value within 0.1 s after discharge, while 80.71 % with a capacitance of 2.34 mF (Figure S16c). After evaluating the recovery rate and instantaneous power output performance, we selected three PANI/CNT fibers as partners for ten biofuel cell fibers twisted together to obtain the complete fiber BSC.

The pulse discharge performance of fiber BSC was evaluated by applying different pulse current values ranging from 0.05 to 5 mA for 10 ms in a 4 mM glucose solution. After each pulse of varying intensity, fiber BSC could deliver power by using stored charges, and quickly recovered to its initial voltage due to the constant spontaneous redox of glucose and oxygen (Figure 2g). The overlay of the peak potential drop demonstrated more clearly the typical pulse discharge process on fiber BSC. It initially experienced a rapid ohmic drop upon the application of current pulse, and then a subsequent slower voltage drop from the capacitive discharge (Figure 2h). Within the multi-stranded twisted fiber BSC, sufficient contact points and microchannels between fiber electrodes provided efficient mass and electron transfer pathways, reducing internal resistance and interfacial impedance of the device (Figure S17). Due to the excellent conductivity of CNT fibers and the advantages brought by the twisting structure, the overall resistance of the hybrid device was only 1.2 $\Omega\,cm^2$ [calculated by Eq. (S1)], which was much lower than 45–75 $\Omega\,cm^2$ of the previous reports.[11b,c] This resulted in a modest ohmic drop and a substantial voltage for pulse discharge. Fiber BSC could withstand high discharge current density of 106.2 $mA\,cm^{-2}$ and achieve maximal power density of 22.6 $mW\,cm^{-2}$ [calculated by Eq. (S2)] at 4 mM glucose concentration matching the physiological range (3.9–7.8 mM) (Figure 2i), much exceed the previous reports (Figure 2j). Furthermore, fiber BSC was able to maintain a stable voltage drop and return swiftly to the initial voltage after applying 0.5 mA current pulse every 30 s (Figure 2k, inset plot). The power output of fiber BSC was consistently maintained at more than 90 % of the initial value after 8460 pulse discharge for three days (Figure 2k), indicating its favorable promise for long-term operation.

The environment in living body is complex and variable,[28] constantly accompanied by inevitable physical movements. It is essential for implanted devices to operate with maximal stability against external fluctuations. In order to confirm the deformation stability of the fiber BSC, the dynamic environmental changes were simulated by friction and bending. Specifically, a 3 wt % agarose gel was used to simulate skin tissue for its similar mechanical properties, and the fiber BSC was passed back and forth across the gel to test its frictional stability (Figure 3a). The results showed that the power density of the PVA-coated device remained above 90 % of its initial value after 2000 cycles of frictions (Figure 3b), while the performance of the device without PVA coating quickly dropped below 90 % after just 300 cycles of frictions due to the possible catalyst shedding (Figure S18). The impedance plot (Figure 3c) and SEM images (Figure S19) further illustrated the high stability of the fiber BSC since no clear fractures were observed owing

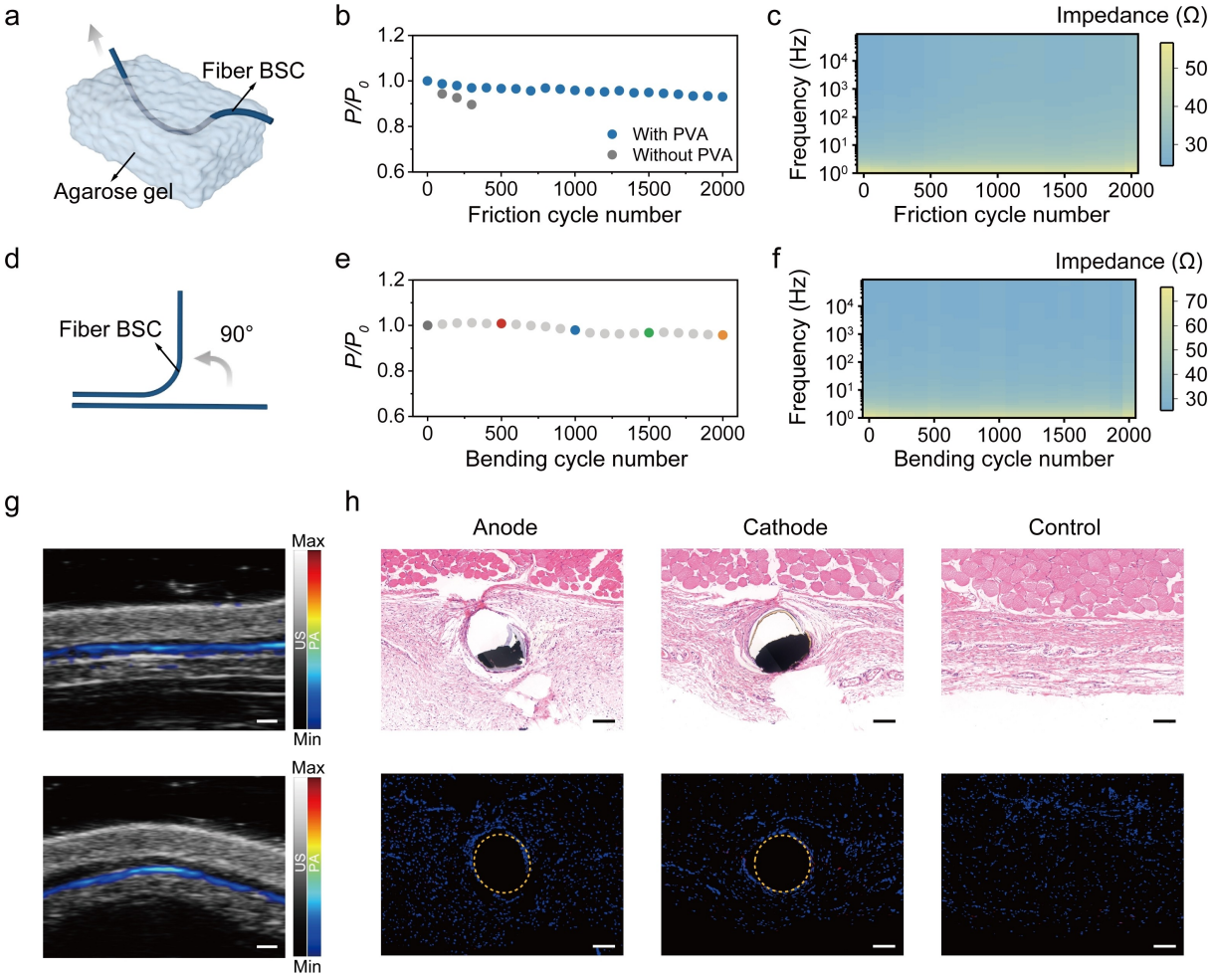

Figure 3. Stability and biocompatibility of fiber BSC. a) Schematic diagram for friction test by putting fiber BSC across agarose gel. b) The relative change in the pulse power density of fiber BSC during 2000 cycles of frictions. c) The evolution of impedance magnitude of fiber BSC during 2000 cycles of frictions. d) Schematic diagram for bending test of fiber BSC. e) The relative change in the pulse power density of fiber BSC during 2000 bending cycles. f) The evolution of impedance magnitude of fiber BSC during 2000 bending cycles. g) Photoacoustic and ultrasonic images of subcutaneous tissue of rat implanted with fiber BSC before (top) and after (bottom) bending. Contour lines were extracted from the images. Scale bar, 500 μm. h) H&E and immunohistochemical staining images of rat subcutaneous tissue after one-week implantation of fiber BSC. Blue and red colors correspond to DAPI (marker of nucleus) and CD68 (marker of macrophage), respectively. Orange dashed circles indicate the position of fiber electrodes. Scale bar, 100 μm. $n=3$ biologically independent experiments for each group.

to the protection of PVA. Moreover, after 2000 bending cycles (Figure 3d), the power density of the fiber BSC also remained above 90% (Figure 3e) and the impedance magnitude changed negligibly (Figure 3f), indicating excellent output stability under dynamic environments.

In addition, the implanted device should not interfere with the normal activity of the tissue. To verify the adaptability of the fiber BSC to physiological activities, ultrasonic photoacoustic imaging was used to visually evaluate the fiber BSC/tissue interface before and after deformation. It was observed that the implanted fiber BSC was able to bend along with the subcutaneous tissue which was deformed by compression on both sides, maintaining a stable device/tissue interface (Figure 3g). Biocompatibility was also systematically investigated to ensure the high safety of implanted devices in vivo. Hematoxylin-eosin (H&E) and immunohistochemical staining were performed one week after the subcutaneous implantation of fiber BSCs in rats (Figure 3h). The results showed that there was no significant macrophage aggregation or inflammatory response around the implanted fiber BSCs compared to the control group. Moreover, H&E staining of major organs (heart, liver, spleen, lung and kidney) of the rats was performed and no obvious pathological changes or tissue damage occurred (Figure S20).

To demonstrate the actual operation of fiber BSC in vivo, it was implanted into subcutaneous tissue of rats to test pulse discharge performances (Figure S21). Due to the unique one-dimensional characteristics and high flexibility of fiber BSC, it could be minimally and invasively implanted into various regions by syringe injection[29] or suture stitching (Figure 4a). The pulsed output was tested by applying current values of 0.05–2 mA for 10 ms. Similar pulsed output profiles were observed (Figure 4b, c) and the maximal

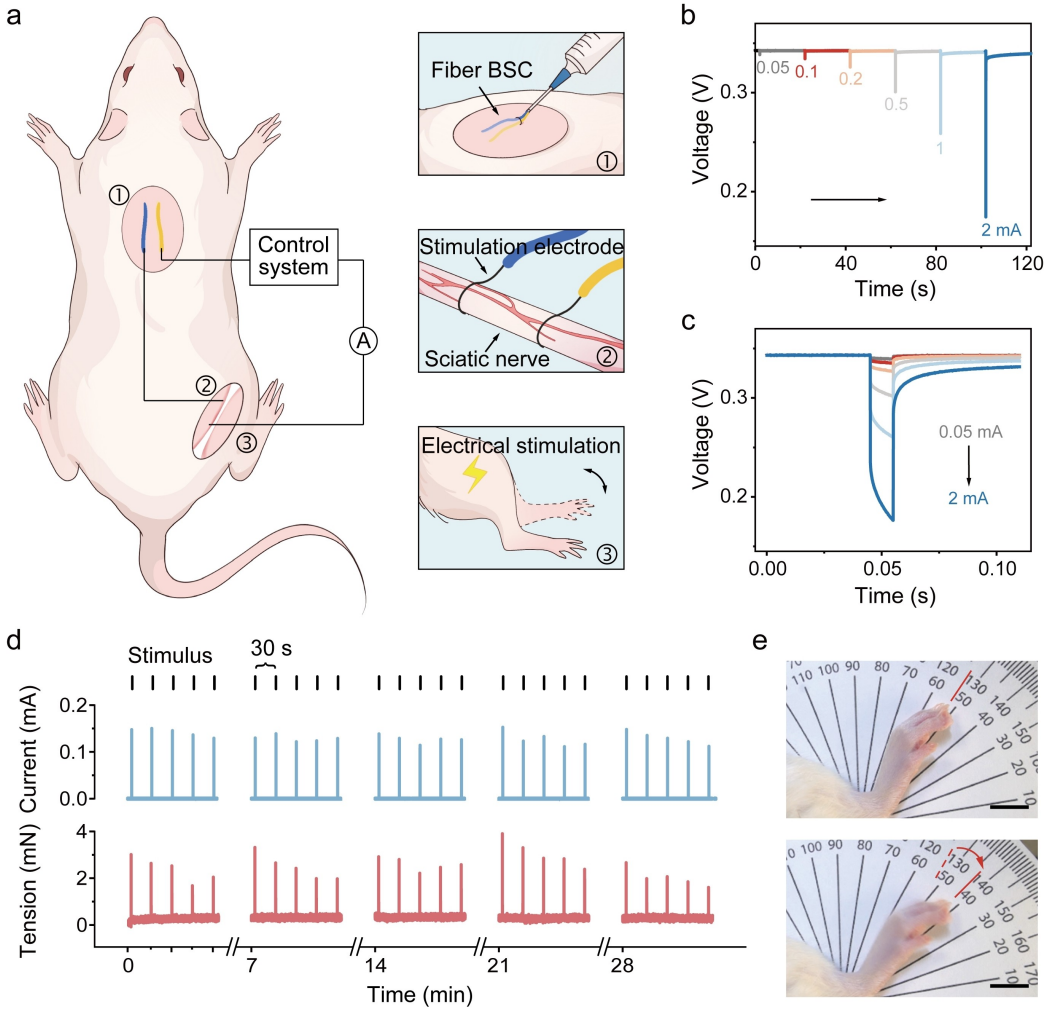

Figure 4. Electrochemical property and application of fiber BSC in vivo. a) Schematic diagram of device implantation and electrical stimulation of the sciatic nerve in a rat. b) Pulse discharge curves at current values of 0.05–2 mA. c) Overlays of pulse discharge curves at (b) for fiber BSC implanted in vivo. d) Recordings of stimulation current and muscle tone in the rat leg during electrical stimulation of sciatic nerve. e) Photographs of the rat leg before (top) and after (bottom) electrical stimulation of sciatic nerve. Scale bar, 1 cm. $n=3$ biologically independent experiments.

power density of fiber BSC in vivo was 7.5 mW cm^{-2} at 2 mA (Figure S22).

Electrical stimulation is a common therapeutic tool to restore motor function of muscles or nerves.[30] A relatively high stimulation current is an essential element to construct effective contraction of the diseased muscle, which requires a strong power supply. In this regard, fiber BSC was well-suited as an implantable energy device for stimulation (Figure 4a). As a proof of concept, the implanted fiber BSC electrodes were connected to both ends of the rat sciatic nerve (Figure S23a), and the rat leg was attached to a tension sensor to record its movement. A wireless control system connected in the middle was used to switch the current pulse (Figure S23b). Under each pulse, the rat leg was able to swing with an amplitude of about 10° (Figure 4e), showing the effectiveness and reproducibility of electrical stimulation. The discharge current of fiber BSC was about 150 μA, and the transducer could repeatedly detect a force of about 3 mN in 5 sets of interval stimulation recordings (Figure 4d). These results demonstrated that fiber BSC could be promisingly used as a high-performance energy system in vivo.

Conclusion

In summary, we developed an implantable fiber BSC by simply twisting multi-stranded fiber biofuel cell and supercapacitor electrodes. The maximal instantaneous power density of the fiber BSC reached 22.6 mW cm^{-2} at current density of 106.2 mA cm^{-2}, with relative stability after 8460 pulse discharge for three days. The entire device exhibited promising properties suitable for implantation, including both high mechanical stability and biocompatibility. Fiber BSC implanted subcutaneously maintained a similar output performance as in vitro. Finally, this fiber BSC was successfully used as an energy source in vivo for neural stimulation to evoke muscle contraction, illustrating its great

potential as an implantable energy system with high power and large current output. This simple fiber twisting strategy promoted efficient mass diffusion and charge transfer among different fibers, which may be a versatile way applicable to other fiber electronics for high performances and multifunctional integration, such as the composite devices of biofuel cells and chemical batteries, solar cells and supercapacitors, as well as self-powered sensors.

Acknowledgements

This work was supported by NSFC (52122310, 22075050), STCSM (21511104900, 20JC1414902), CPSF (BX2021074), Shanghai Municipal Science and Technology Major Project (2018SHZDZX01), ZJ Lab, and Shanghai Center for Brain Science and Brain-Inspired Technology.

Conflict of Interest

The authors declare no conflict of interest.

Data Availability Statement

The data that support the findings of this study are available from the corresponding author upon reasonable request.

Keywords: Biofuel Cell · Biosupercapacitors · Fiber · Implantable Electronics

[1] a) Z. Lv, W. Li, J. Wei, F. Ho, J. Cao, X. Chen, *CCS Chem.* **2023**, *5*, 11–29; b) Z. Lv, C. Wang, C. Wan, R. Wang, X. Dai, J. Wei, H. Xia, W. Li, W. Zhang, S. Cao, F. Zhang, H. Yang, X. Loh, X. Chen, *Adv. Mater.* **2022**, *34*, 2202877.

[2] a) L. Halámková, J. Halámek, V. Bocharova, A. Szczupak, L. Alfonta, E. Katz, *J. Am. Chem. Soc.* **2012**, *134*, 5040–5043; b) T. Miyake, K. Haneda, N. Nagai, Y. Yatagawa, H. Onami, S. Yoshino, T. Abe, M. Nishizawa, *Energy Environ. Sci.* **2011**, *4*, 5008–5012.

[3] a) G. Pankratova, D. Pankratov, K. Hasan, H.-E. Akerlund, P.-A. Albertsson, D. Leech, S. Shleev, L. Gorton, *Adv. Energy Mater.* **2017**, *7*, 1602285; b) Y. Jang, T. Park, E. Kim, J. W. Park, D. Y. Lee, S. J. Kim, *Angew. Chem. Int. Ed.* **2021**, *60*, 10563–10567.

[4] a) C. Agnès, M. Holzinger, A. Le Goff, B. Reuillard, K. Elouarzaki, S. Tingry, S. Cosnier, *Energy Environ. Sci.* **2014**, *7*, 1884–1888; b) G. Pankratova, P. Bollella, D. Pankratov, L. Gorton, *Curr. Opin. Biotechnol.* **2022**, *73*, 179–187.

[5] a) D. Pankratov, Z. Blum, D. B. Suyatin, V. O. Popov, S. Shleev, *ChemElectroChem* **2014**, *1*, 343–346; b) X. Xiao, P. O. Conghaile, D. Leech, R. Ludwig, E. Magner, *Biosens. Bioelectron.* **2017**, *98*, 421–427; c) P. Liang, C. Zhang, Y. Jiang, Y. Bian, H. Zhang, X. Sun, X. Yang, X. Zhang, X. Huang, *Appl. Energy* **2017**, *185*, 582–588.

[6] S. Shleev, E. Gonzalez-Arribas, M. Falk, *Curr. Opin. Electrochem.* **2017**, *5*, 226–233.

[7] a) J. Lv, L. Yin, X. Chen, I. Jeerapan, C. A. Silva, Y. Li, M. Le, Z. Lin, L. Wang, A. Trifonov, S. Xu, S. Cosnier, J. Wang, *Adv. Funct. Mater.* **2021**, *31*, 2102915; b) J. Lv, I. Jeerapan, F. Tehrani, L. Yin, C. A. Silva-Lopez, J.-H. Jang, D. Joshuia, R. Shah, Y. Liang, L. Xie, F. Soto, C. Chen, E. Karshalev, C. Kong, Z. Yang, J. Wang, *Energy Environ. Sci.* **2018**, *11*, 3431–3442.

[8] a) M. Kizling, S. Draminska, K. Stolarczyk, P. Tammela, Z. Wang, L. Nyholm, R. Bilewicz, *Bioelectrochemistry* **2015**, *106*, 34–40; b) P. Bollella, Z. Boeva, R.-M. Latonen, K. Kano, L. Gorton, J. Bobacka, *Biosens. Bioelectron.* **2021**, *176*, 112909.

[9] D. Jiang, B. Shi, H. Ouyang, Y. Fan, Z. L. Wang, Z. Li, *ACS Nano* **2020**, *14*, 6436–6448.

[10] S.-Y. Yang, V. Sencadas, S. S. You, N. Z.-X. Jia, S. S. Srinivasan, H.-W. Huang, A. E. Ahmed, J. Y. Liang, G. Traverso, *Adv. Funct. Mater.* **2021**, *31*, 2009289.

[11] a) D. Pankratov, F. Conzuelo, P. Pinyou, S. Alsaoub, W. Schuhmann, S. Shleev, *Angew. Chem. Int. Ed.* **2016**, *55*, 15434–15438; b) C. W. Narvaez Villarrubia, F. Soavi, C. Santoro, C. Arbizzani, A. Serov, S. Rojas-Carbonell, G. Gupta, P. Atanassov, *Biosens. Bioelectron.* **2016**, *86*, 459–465; c) X. Xiao, P. O. Conghaile, D. Leech, R. Ludwig, E. Magner, *Biosens. Bioelectron.* **2017**, *90*, 96–102; d) T. Bobrowski, E. G. Arribas, R. Ludwig, M. D. Toscano, S. Shleev, W. Schuhmann, *Biosens. Bioelectron.* **2018**, *101*, 84–89; e) H.-J. Kil, S.-R. Kim, J.-W. Park, *ACS Appl. Mater. Interfaces* **2022**, *14*, 3838–3848; f) C. Hou, A. Liu, *Electrochim. Acta* **2017**, *245*, 295–300.

[12] X. Xiao, H.-Q. Xia, R. Wu, L. Bai, L. Yan, E. Magner, S. Cosnier, E. Lojou, Z. Zhu, A. Liu, *Chem. Rev.* **2019**, *119*, 9509–9558.

[13] A. Zebda, J.-P. Alcaraz, P. Vadgama, S. Shleev, S. D. Minteer, F. Boucher, P. Cinquin, D. K. Martin, *Bioelectrochemistry* **2018**, *124*, 57–72.

[14] a) P. N. Bartlett, F. A. Al-Lolage, *J. Electroanal. Chem.* **2018**, *819*, 26–37; b) A. J. Bandodkar, P. Gutruf, J. Choi, K. Lee, Y. Sekine, J. T. Reeder, W. J. Jeang, A. J. Aranyosi, S. P. Lee, J. B. Model, R. Ghaffari, C.-J. Su, J. P. Leshock, T. Ray, A. Verrillo, K. Thomas, V. Krishnamurthi, S. Han, J. Kim, S. Krishnan, T. Hang, J. A. Rogers, *Sci. Adv.* **2019**, *5*, eaav3294.

[15] Y. Guo, C. Chen, J. Feng, L. Wang, J. Wang, C. Tang, X. Sun, H. Peng, *Small Methods* **2022**, *6*, 2200142.

[16] X. Fu, Z. Li, L. Xu, M. Liao, H. Sun, S. Xie, X. Sun, B. Wang, H. Peng, *Sci. China Mater.* **2019**, *62*, 955–964.

[17] a) C. Chen, J. Feng, J. Li, Y. Guo, X. Shi, H. Peng, *Chem. Rev.* **2023**, *123*, 613–662; b) C. H. Kwon, S.-H. Lee, Y.-B. Choi, J. A. Lee, S. H. Kim, H.-H. Kim, G. M. Spinks, G. G. Wallace, M. D. Lima, M. E. Kozlov, R. H. Baughman, S. J. Kim, *Nat. Commun.* **2014**, *5*, 3928.

[18] B. Shi, Z. Li, Y. Fan, *Adv. Mater.* **2018**, *30*, 1801511.

[19] D. P. Dubal, O. Ayyad, V. Ruiz, P. Gomez-Romero, *Chem. Soc. Rev.* **2015**, *44*, 1777–1790.

[20] C. Y. Chan, Z. Wang, H. Jia, P. F. Ng, L. Chow, B. Fei, *J. Mater. Chem. A* **2021**, *9*, 2043–2069.

[21] Y. Yang, Y. Su, X. Zhu, D. Ye, R. Chen, Q. Liao, *Biosens. Bioelectron.* **2022**, *198*, 113833.

[22] a) X. Kang, Z. Zhu, T. Zhao, W. Zhai, J. Xu, Z. Lin, K. Zeng, B. Wang, X. Sun, P. Chen, H. Peng, *Adv. Funct. Mater.* **2022**, *32*, 2207763; b) T. Jing, B. Xu, J. H. Xin, X. Guan, Y. Yang, *J. Mater. Chem. A* **2021**, *9*, 12331–12339; c) C.-e. Zhao, P. Gai, R. Song, Y. Chen, J. Zhang, J.-J. Zhu, *Chem. Soc. Rev.* **2017**, *46*, 1545–1564.

[23] B.-A. Mei, O. Munteshari, J. Lau, B. Dunn, L. Pilon, *J. Phys. Chem. C* **2018**, *122*, 194–206.

[24] a) Z. Lv, D. Xie, F. Li, Y. Hu, C. Wei, C. Feng, *J. Power Sources* **2014**, *246*, 642–649; b) C. Feng, Z. Lv, X. Yang, C. Wei, *Phys. Chem. Chem. Phys.* **2014**, *16*, 10464–10472.

[25] F. Conzuelo, N. Markovic, A. Ruff, W. Schuhmann, *Angew. Chem. Int. Ed.* **2018**, *57*, 13681–13685.

[26] C. Meng, C. Liu, L. Chen, C. Hu, S. Fan, *Nano Lett.* **2010**, *10*, 4025–4031.

[27] S. Alsaoub, F. Conzuelo, S. Gounel, N. Mano, W. Schuhmann, A. Ruff, *ChemElectroChem* **2019**, *6*, 2080–2087.
[28] D. Zhang, Q. Chen, C. Shi, M. Chen, K. Ma, J. Wan, R. Liu, *Adv. Funct. Mater.* **2021**, *31*, 2007226.
[29] J. Liu, T.-M. Fu, Z. Cheng, G. Hong, T. Zhou, L. Jin, M. Duvvuri, Z. Jiang, P. Kruskal, C. Xie, Z. Suo, Y. Fang, C. M. Lieber, *Nat. Nanotechnol.* **2015**, *10*, 629–636.
[30] a) S. He, A. Zhang, D. Wang, H. Song, H. Chu, F. Ni, Y. Zhang, P. Chen, B. Zhang, L. Qiu, H. Peng, *Chem. Eng. J.* **2022**, *441*, 136106; b) T. Schauer, *Annu. Rev. Control* **2017**, *44*, 355–374.

Manuscript received: March 4, 2023
Accepted manuscript online: May 16, 2023
Version of record online: May 16, 2023